Tungsten Sulfide Enhancing Solar-Driven Hydrogen Production from Silicon Nanowires

Zhipeng Huang,*,[†] Chifang Wang,[†] Zhibo Chen,[†] Hua Meng,[‡] Cuncai Lv,[†] Zhongzhong Chen,[†] Ruqu Han,[§] and Chi Zhang*,[†]

[†]China-Australia Joint Research Center for Functional Molecular Materials, Scientific Research Academy, Jiangsu University, Zhenjiang, Jiangsu 212013, People's Republic of China

[‡]Research Institute of Refrigeration and Thermal Engineering, College of Mechanical Engineering, Tongji University, Shanghai 200092, People's Republic of China

[§]Department of Physics, Jiangsu University of Science and Technology, Zhenjiang, Jiangsu 212003, People's Republic of China

S *Supporting Information*

ABSTRACT: Tungsten sulfides, including WS_2 (crystalline) and WS_3 (amorphous), were introduced to silicon nanowires, and both can promote the photoelectrochemical hydrogen production of silicon nanowires. In addition, more enhancement of energy conversion efficiency can be achieved by the loading of WS_3, in comparison with loading of WS_2. Polarization curves of WS_3 and WS_2 suggest that WS_3 has higher catalytic activity in the hydrogen evolution reaction than WS_2, affording higher energy conversion efficiency in silicon nanowires decorated with WS_3. The higher electrocatalytic activity of WS_3 correlates with the amorphous structure of WS_3 and larger surface area of WS_3, which result in more active sites in comparison with crystalline WS_2.

KEYWORDS: silicon nanowires, tungsten sulfide, hydrogen evolution reaction, photoelectrochemical
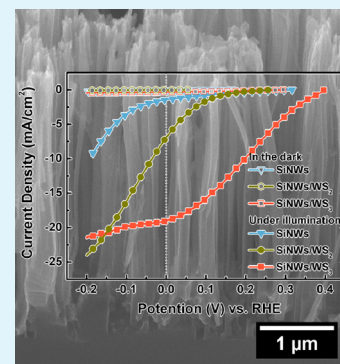
1. INTRODUCTION

Photoelectrochemically splitting water to hydrogen (H_2) and oxygen (O_2) accomplishes simultaneously the harvesting of solar energy and the storage of solar energy into a clean chemical fuel (H_2), and therefore is gaining extensive and increasing attention with respect to the global energy crisis and environmental issues.[1] In principle, a promising photocathode with efficient H_2 generation capability in a photoelectrochemical water splitting cell should be able to sufficiently utilize the solar spectrum, and should have fast hydrogen evolution reaction (HER) kinetics so that photogenerated electrons in the photocathode can effectively reduce species in electrolyte into H_2 instead of recombining with photogenerated holes.

Silicon (Si) can absorb photons with wavelengths ranging from UV to near IR, and has been widely applied in the field of solar energy conversion, including solar cell and photoelectrochemical water splitting.[2,3] It is further demonstrated that one-dimensional Si nanostructures (Si nanowires, SiNWs) can improve the absorption capability and therefore power conversion efficiency, in comparison with their bulk counterpart.[4−6] However, similar to other semiconductors, the intrinsic HER kinetics of Si is slow. This shortage results in the low energy conversion efficiency (η) of a photocathode constructed from native bulk Si or SiNWs.

Introducing a HER electrocatalyst to the Si surface can improve the HER kinetics of Si-based photocathodes, and this configuration has been investigated for several decades.[2] However, the widely used and high performance HER electrocatalysts are expensive and rare earth metals (e.g., Pt[2]). Consequently, the practical application of such catalysts in photocathodes is limited. Although various nonprecious HER electrocatalysts have been reported, only a limited amount of them have been applied to photocathodes, including Ni−Mo alloy,[7] NiO_x,[8] Mo_3S_4 cluster,[9] MoS_2 film,[10] and MoS_3 particles.[11]

On the other hand, although the application of tungsten sulfide in HER has been demonstrated, including in electrocatalysis[12,13] and photocatalysis,[14,15] the application of tungsten sulfide in photocathodes has not yet been reported. Furthermore, the research concerning HER catalytic activity of tungsten sulfide is focused on the development of various morphologies of tungsten sulfide.[16−18] The influence of structure and/or chemical composition of tungsten sulfide on its HER catalytic activity has not been explored.

In this article, the systematic investigation on the photoelectrochemical hydrogen production capabilities of SiNWs decorated with tungsten sulfides is introduced. Two kinds of tungsten sulfides, including WS_3 (amorphous) and WS_2

(crystalline) have been deposited onto SiNWs by convenient drop coating and pyrolysis methods. The two tungsten sulfides can both improve the η of SiNWs, whereas the η of SiNWs loaded with WS_3 (denoted as SiNWs/WS_3) is 11 times that of SiNWs loaded with WS_2 (denoted as SiNWs/WS_2), and 24 times that of SiNWs. Electrochemical impedance spectroscopy (EIS) investigation on SiNWs, SiNWs/WS_3, and SiNWs/WS_2, as well as polarization curves of WS_3 and WS_2 loaded on a glass carbon electrode (GCE), suggest that the enhanced photoelectrochemical hydrogen production capability of SiNWs/WS_3 and SiNWs/WS_2 can be attributed to the electrocatalytic activity of WS_3 and WS_2, and that the superior catalytic activity of WS_3 to WS_2 affords the superior performance of SiNWs/WS_3 to SiNWs/WS_2. The superior catalytic activity of WS_3 correlates with its amorphous structure, which can expose more active sites than the crystalline one. These results demonstrate the promising application potential of tungsten sulfide in photoelectrochemical hydrogen production and reveal that the catalytic activity of tungsten sulfide correlates with its microstructure.

2. EXPERIMENTAL SECTION

Fabrication of SiNWs. SiNWs were fabricated via metal-assisted chemical etching (MACE).[19,20] The p-type (100) Si wafers (1−10 Ω· cm) were degreased by ultrasonication in sequence in ethanol and acetone each for 15 min and then rinsed with a copious amount of deionized water. Afterward, the degreased Si substrates were subjected to a boiling solution composed of H_2O_2 and H_2SO_4 (1:4, V:V) for 30 min, followed by deionized water rinsing. In a typical MACE process, the cleaned Si substrates were immersed in an aqueous etchant ($AgNO_3$, 20 mM; HF, 4.5 M) for 30 min at 30 °C. Afterward, silver dendrites covering SiNWs samples were removed by immersion in 5% HNO_3 for 30 min. The SiNWs were rinsed with deionized water and finally dried at 80 °C in air.

Fabrication of WS_3 and WS_2. To fabricate WS_3, $(NH_4)_2WS_4$ powder was loaded in a quartz tube mounted in a tube furnace. The quartz tube was pumped to 20 Pa and filled with high purity nitrogen (99.999%). This procedure was repeated five times prior to pyrolysis. After that, the pyrolysis was carried out at 300 °C for 2 h with flowing 100 sccm high purity nitrogen. Afterward, the tube furnace was cooled naturally to room temperature. The fabrication of WS_2 is similar to that of WS_3, except that the pyrolysis temperature is 500 °C.

Fabrication of SiNWs/WS_3 and SiNWs/WS_2. $(NH_4)_2WS_4$ powder (26 mg, 0.1 mmol) was dispersed in methanol (10 mL) with the aid of ultrasonication. SiNWs substrates were cut into small pieces (8 × 8 mm). In a typical experiment, 20 μL of $(NH_4)_2WS_4$/methanol dispersion was dropped onto a SiNWs sample, and the SiNWs sample was spun at a speed of 600 rpm until methanol was totally evaporated. This speed is sufficiently small to ensure that $(NH_4)_2WS_4$/methanol dispersion can be homogeneously distributed on the surface of SiNWs sample while no dispersion was spun out the sample. Afterward, the SiNWs/$(NH_4)_2WS_4$ sample was subjected to pyrolysis with the same recipe as WS_3 or WS_2, resulting in SiNWs/WS_3 or SiNWs/WS_2, respectively.

Sample Characterization. The morphologies of SiNWs, SiNWs/WS_3, and SiNWs/WS_2 were accessed by scanning electron microscopy (SEM, 7001F, JEOL) equipped with Oxford Instruments' INCA system and transmission electron microscopy (TEM, 2100, JEOL) equipped with GENESIS 2000 XM 30T. For TEM investigation, isolated SiNWs/WS_3 and SiNWs/WS_2 were scratched from corresponding samples, and dispersed in ethanol by ultrasonication. The dispersion was dropped onto carbon-coated copper grid (300 mesh). The copper grid was then dried at 100 °C for 5 min before the TEM characterization.

The X-ray photoelectron spectroscopy (XPS) experiments were carried out on a Physical Electronics PHI 5700 ESCA System equipped with a monochromatic Al Kα (1486.6 eV) source and a concentric hemispherical energy analyzer. Powder X-ray diffraction (XRD) patterns were collected with a D8 ADVANCE instrument with graphite-monochromatized Cu KR radiation (λ = 1.541 78 Å).

Electrochemical Measurement. The photoelectrochemical measurements were carried out in an aqueous 0.05 M H_2SO_4 solution containing 0.5 M K_2SO_4 with an electrochemical workstation (CHI 614D, CH Instrument). A three-electrode configuration was adopted in the measurements, with SiNWs, SiNWs/WS_3, or SiNWs/WS_2 as the working electrode, a graphite rod (6 mm diameter, 100 mm length) as the counter electrode, and a mercury/mercurous sulfate electrode (MSE) as the reference electrode. The reversible hydrogen evolution potential (RHE) was determined by the open circuit potential of a clean Pt electrode in the same solution,[1,6] being −0.762 V vs MSE. Therefore, a potential measured with respect to MSE electrode was referenced to RHE by adding a value of 0.762 V.

SiNWs, SiNWs/WS_3, or SiNWs/WS_2 samples were assembled into a homemade electrochemical cell, with only a defined area (0.07 cm²) of the front surface of sample exposed to solution during measurements. Indium−gallium alloy (99.99%, Sigma-Aldrich) was applied to the back side of SiNWs (or SiNWs/WS_3, SiNWs/WS_2) enabling Ohmic contact. For photoelectrochemical measurements, the illumination was generated by a xenon lamp (350 W), and the incident light density was adjusted to 100 mW/cm² prior to each experiment. Photocurrent density−potential (J−V) relations were measured at a scan rate of 50 mV/s. The open-circuit potential (V_{oc}) and short-circuit current density (J_{sc}) are referenced to RHE, and energy conversion efficiency (η) of photocathode was calculated as $\eta = J_{mp}V_{mp}/P_{in}$, where J_{mp} and V_{mp} are the current density and applied potential at the maximum power point, and P_{in} is the power of incident illumination.[1]

EIS measurements were carried out in three electrode configuration at 0 V vs RHE with applied 5 mV sinusoidal perturbations in the frequency range of 1−10^6 Hz with 12 steps per decade.

For the evaluation of HER catalytic activity, 4 mg of WS_3 (or WS_2) was dispersed in 1 mL of water/ethanol (4/1, V/V) containing 80 μL of Nafion solution (5 wt %). Five milliliters of this dispersion was dropped onto a GCE (diameter 3 mm) and the resulting GCE was dried at 70 °C prior to measurement. The evaluation of the HER catalytic activity of WS_3 (or WS_2) loaded on GCE was carried out by linear sweep voltammetry (5 mV/s) in the same solution used in photoelectrochemical measurements.

The volume of H_2 during potentiostatic electrolysis measurement under illumination (V = 0.1 V vs RHE) was monitored by volume displacement in a configuration shown in Figure S1 (Supporting Information). In this experiment, the backside of SiNWs/WS_3 was connected to a Cu wire with indium−gallium alloy and Ag paste. A Cu wire was threaded to a glass tube (6 mm diameter), and the back side and front side of SiNWs/WS_3 electrode were then sealed with epoxy resin except for an exposed area (~0.5 cm²). A Freescale MPXV7002DP differential pressure transducer was employed to monitor pressure variation in the gas gathering tube, and then the volume of generated H_2 was computed from pressure variation in the gas gathering tube (see details in the Supporting Information). The photocurrent was measured with an electrochemical workstation and the voltage change of the pressure transducer was monitored with a digital multimeter (4 1/2 digit). Prior to the experiment, the relationship between volume of generated H_2 and pressure variation in the gas gathering tube was calibrated by injecting known amounts of air into the gas gathering tube and recording the pressure change.

3. RESULTS AND DISCUSSIONS

SiNWs/WS_3 (amorphous) and SiNWs/WS_2 (crystalline) were fabricated by the combination of drop coating of $(NH_4)_2WS_4$ methanol dispersion onto SiNWs and pyrolysis at desired temperatures (see details in the Experimental Section). The pyrolysis temperature resulting in WS_3 or WS_2 was chosen according to thermogravimetric analysis/differential scanning calorimetry (TGA/DSC) measurement of $(NH_4)_2WS_4$ (Figure S2, Supporting Information). It is shown that the weight loss
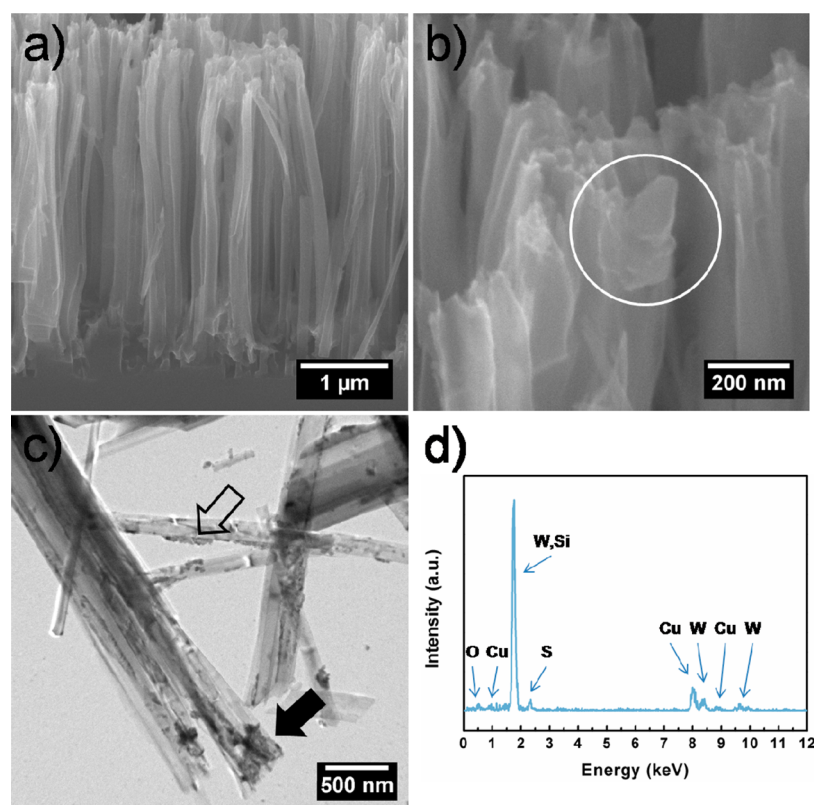
Figure 1. (a) Low and (b) high magnification bird's eye view SEM images of SiNWs/WS$_3$ (sample 45° tilted). (c) TEM image of SiNWs/WS$_3$. (d) EDS spectrum of SiNWs/WS$_3$ recorded in TEM.
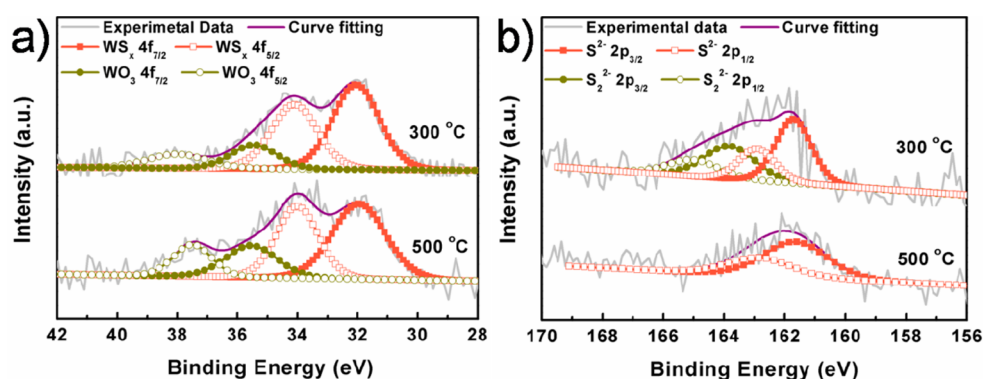

Figure 2. (a) W 4f window of XPS spectra and (b) S 2p window of XPS spectra.

was 17.6% when the sample was heated up to 300 °C, matching well that of the reaction $(NH_4)_2WS_4 \rightarrow WS_3 + 2NH_3 + H_2S$, and the weight loss at 500 °C (28.7%) is similar to that of the reaction $(NH_4)_2WS_4 \rightarrow WS_2 + S + 2NH_3 + H_2S$ (29%). Therefore, the pyrolysis temperatures were set to 300 °C for the fabrication of SiNWs/WS$_3$ and 500 °C for that of SiNWs/WS$_2$

The morphologies of SiNWs/WS$_3$ and SiNWs/WS$_2$ were accessed by SEM. The two samples exhibit similar morphologies. Figure 1a shows a representative bird's eye view SEM image of SiNWs/WS$_3$. SiNWs exhibit a typical morphology as those resulted from MACE, possessing ca. 5 μm length and 20−200 nm diameter. On the top part of the SiNWs, WS$_3$ particles can be found (indicated by circle in Figure 1b). The distribution of WS$_3$ on SiNWs was revealed by elemental line profiles recorded in SEM (Figure S3, Supporting Information). The line profiles suggest that WS$_3$ locates mainly on the top of

SiNWs, and with the distance from the top of SiNWs increasing, the amount of WS$_3$ decreases. The morphological feature can be further confirmed by TEM characterization (Figure 1c). The component with a darker contrast, being assigned as WS$_3$, can be found on the top part (solid arrow in Figure 1c), and the side wall (open arrow in Figure 1c) of SiNWs, respectively. A typical energy dispersive spectroscopy (EDS) experiment carried out in TEM confirms the presence of W and S on SiNWs (Figure 1d).

A series of experiments were carried out to further investigate the structural, compositional, and chemical information on tungsten sulfides fabricated at 300 and 500 °C. For these experiments, $(NH_4)_2WS_4$ was pyrolyzed without being deposited onto SiNWs. Atomic ratios of W to S in the two samples were averaged from five EDS spectra recorded from different regions of corresponding samples from SEM (Figure S4 and Table S1, Supporting Information), respectively. It is

shown that S:W is 3.00 ± 0.13 in the sample pyrolyzed at 300 °C, and is 2.03 ± 0.08 in that at 500 °C. These values suggest that $(NH_4)_2WS_4$ decomposes into WS_3 at 300 °C, and evolves to WS_2 at 500 °C, in accordance with those suggested by TGA/DSC experiments.

Detailed chemical states of W and S were obtained from XPS characterization. Figure 2a shows the W 4f window of XPS spectra of samples pyrolyzed at 300 and 500 °C. The spectra of the two samples show two doublets with W $4f_{7/2}$ binding energies at 32.0 and 35.4 eV. The peak with binding energy of 35.4 eV can be assigned to W in WO_3, whereas the peak with a binding energy of 32.0 eV comes from W in WS_2 or WS_3.[21] On the other hand, samples pyrolyzed at 300 and 500 °C exhibit different S 2p windows of XPS spectra. The S 2p window of the sample pyrolyzed at 300 °C has two doublets, 161.7 and 163.8 eV, whereas only one doublet peaking at 161.7 eV can be found in S 2p windows of samples pyrolyzed at 500 °C (Figure 2b). The doublet peaking at 161.7 eV indicates S^{2-} ligands, which come from WS_2 or WS_3. The peak with binding energy of 163.8 eV can be attributed to bridging S_2^{2-} or apical S^{2-}. Although it is difficult to exclusively identify the ratio between these sulfur species due to their similar binding energies, the presence of S_2^{2-} bridging or apical S^{2-} suggests the formation of WS_3.[21] In addition, XPS spectra of the O 1s window show two peaks at 533.2 and 531.8 eV (Figure S5, Supporting Information), in accordance with those of O in partially sulfidized WO_3.[22] The peak at the low energy can be assigned to the oxide, and the high energy one to hydroxide forms.[22] According to XPS investigation, the sample pyrolyzed at 500 °C contains WS_2 and WO_3, and that at 300 °C contains WS_3 and WO_3. The WO_3 might come from surface oxidation of sulfides with the exposure of samples in air. Hereafter, the sample pyrolyzed at 300 °C will be termed in brief as WS_3 and that at 500 °C as WS_2, because WO_3 has no electrocatalytic activity.[15]

The overall structural features of WS_3 and WS_2 were accessed via X-ray diffraction (XRD) experiments (Figure 3a). The experimental patterns of WS_2 exhibit distinct peaks, suggesting
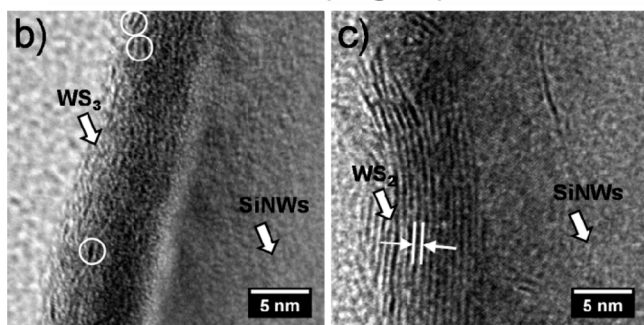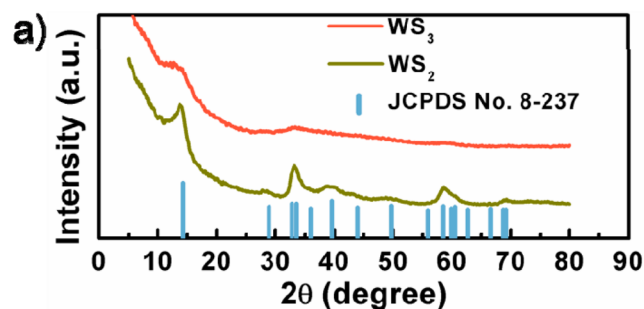
the crystalline nature of the products. These peaks match well those from hexagonal phase WS_2 (JCPDS No. 8-237, $a = 0.315$ nm, $c = 1.2362$ nm). In contrast, only a broad shoulder at 14.3° can be found in XRD patterns of WS_3, suggesting that WS_3 is amorphous with short-range ordering. In addition, no peaks from WO_3 can be found, suggesting that the amount of WO_3 is relatively small. This is in accordance with the deduction that WO_3 found by XPS experiments were formed only on the surface of WS_2 and WS_3.

To assess the detailed microstructures of $SiNWs/WS_3$ and $SiNWs/WS_2$, high resolution TEM (HRTEM) experiments were carried out. Figure 3b shows the typical HRTEM image of $SiNWs/WS_3$, in which SiNWs and WS_3 have been indicated by arrows, respectively. No well-defined lattice fringe can be found from WS_3. A close examination of WS_3 reveals the short-range ordering of atoms on some tiny regions (~2 nm diameter), as indicated by white circles in Figure 3b. In these regions, fringes with 0.62 nm can be found. This value is associated with the shoulder (14.3°) found in XRD experiments (Figure 3a). According to XRD and TEM observations, WS_3 is amorphous whereas a short-range layer structure is formed. Figure 3c shows the morphology of $SiNWs/WS_2$. A well-defined layer structure suggests the good crystallinity of WS_2. The distance between fringes is 0.62 nm, matching well that of (002) plane in hexagonal phase WS_2 (JCPDS No. 8-237).

The photoelectrochemical hydrogen production capabilities of SiNWs, $SiNWs/WS_3$, and $SiNWs/WS_2$ were evaluated via polarization experiments. The corresponding current density (J)-potential (V) relations measured in the dark and under illumination are shown in Figure 4. The SiNWs exhibit the
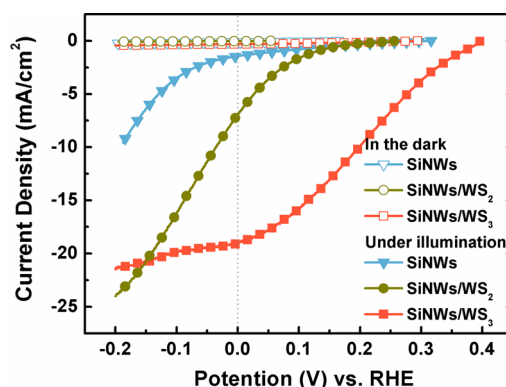
Figure 3. (a) XRD patterns of WS_3 and WS_2. TEM images of (b) $SiNWs/WS_3$ and (c) $SiNWs/WS_2$.

Figure 4. $J-V$ relations of SiNWs, $SiNWs/WS_3$, and $SiNWs/WS_2$ measured under illumination (100 mW/cm²) and in the dark.

smallest J_{sc} (1.4 mA/cm²) and the V_{oc} is 0.3 V. The deposition of WS_3 and WS_2 on SiNWs can remarkably enhance the photoresponse of SiNWs. The J_{sc} of $SiNWs/WS_2$ is increased to 7.0 mA/cm², and the J_{sc} of $SiNWs/WS_3$ is increased to 19.0 mA/cm². Besides J_{sc}, V_{oc} of $SiNWs/WS_3$ (0.40 V) is larger than that of $SiNWs/WS_2$ (0.26 V) and SiNWs. The η of samples were calculated according to the equation listed in the Experimental Section, being 0.0845% ($V_{mp} = 0.12$ V vs RHE, $J_{mp} = 0.704$ mA/cm²) for SiNWs, 2.02% ($V_{mp} = 0.179$ V vs RHE, $J_{mp} = 11.3$ mA/cm²) for $SiNWs/WS_3$, and 0.187% ($V_{mp} = 0.062$ V vs RHE, $J_{mp} = 3.02$ mA/cm²) for $SiNWs/WS_2$.

Table S2 (Supporting Information) summarizes the key performances of recently reported Si-based photocathodes. It is found that the η of $SiNWs/WS_3$ is larger than that of silicon microwires (SiMWs) decorated with Mo_3S_4 clusters (1.24%),[9]
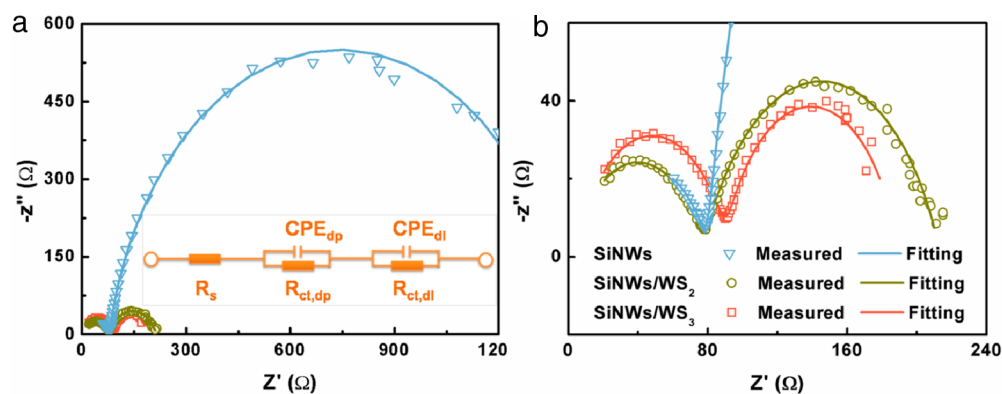
Figure 5. EIS spectra of SiNWs, SiNWs/WS$_3$, and SiNWs/WS$_2$. (a) Nyquist plot of EIS spectra measured from SiNWs, SiNWs/WS$_3$, and SiNWs/WS$_2$ at $V = 0$ V vs RHE under illumination (100 mW/cm^2). (b) A detail plot of EIS spectra in (a) at small impedance region.

SiNWs decorated with a MoS$_2$ shell (0.03%),[23] and p-SiMWs decorated with Pt particles (0.21%),[6] and is 75% of that of SiNWs decorated with Pt particles (2.73%).[24] The η of SiNWs/WS$_3$ could be further increased by introduction of an n^+ layer to the surface of SiNWs.[6] These comparisons demonstrate the promising application of SiNWs/WS$_3$ in photoelectrochemical hydrogen production.

It is worth noting that the loading amounts of precursor ((NH$_4$)$_2$WS$_4$) on SiNWs in SiNWs/WS$_3$ and SiNWs/WS$_2$ are identical. Consequently, the prominent difference in photo-electrochemical performances should not be associated with the loading amount of WS$_3$ and WS$_2$. To clarify the origin of performance enhancement in SiNWs/WS$_3$ in comparison with SiNWs and SiNWs/WS$_2$, systematic experiments were carried out.

Diffuse UV−vis experiments (Figure S6, Supporting Information) reveal that the three samples (SiNWs, SiNWs/WS$_2$, and SiNWs/WS$_3$) exhibit nearly identical reflectance in the wavelength range of 300−1100 nm, excluding the possibility that different performances of SiNWs, SiNWs/WS$_3$, and SiNWs/WS$_2$ origin from the absorption ability of different samples. It is therefore reasonable to attribute the different performances between SiNWs/WS$_3$, SiNWs/WS$_2$, and SiNWs to different HER activities between WS$_3$ and WS$_2$.

The difference in catalytic activities of SiNWs/WS$_3$ and SiNWs/WS$_2$ was also suggested by EIS measurements. The EIS spectra of SiNWs, SiNWs/WS$_3$, and SiNWs/WS$_2$ measured at 0 V vs RHE are presented in Nyquist plots (scatters in Figure 5), where the x-axis is the real part of impedance and the y-axis is the image part. Each spectrum contains two semicircles, in accordance with two capacitance elements presented in the working electrode (i.e., depletion layer in SiNWs, and double layer in electrolyte near photocathode/electrolyte interface). The semicircle in the high frequency range is assigned to the capacitance of the depletion layer in SiNWs, and the one in low frequency range to the capacitance of the double layer.[25]

The EIS data are fitted to the equivalent circuit shown in the inset of Figure 5a, where R_s represents the overall series resistance of the circuit, CPE$_{dp}$ is the capacitance phase element for the depletion layer of SiNWs, $R_{ct,dp}$ is the charge transfer resistance in the depletion layer of semiconductor, CPE$_{dl}$ is the capacitance phase element for the double layer at the photocathode/electrolyte interface, and $R_{ct,dl}$ is the charge transfer resistance of the double layer at the photocathode/electrolyte interface. The $R_{ct,dl}$ is correlated to the kinetics of Faradaic reaction across the double layer (i.e., the reduction of

H$^+$ to hydrogen in our experiments), with a smaller value, corresponding to a faster reaction rate.[26] Semicircles in the low frequency range corresponding to SiNWs/WS$_3$ and SiNWs/WS$_2$ have smaller diameters (Figure 5b) than that of SiNWs, implying that the introduction of WS$_3$ and WS$_2$ can reduce the $R_{ct,dl}$ of the photocathode. In addition, the semicircle in the low frequency range corresponding to SiNWs/WS$_3$ has a smaller diameter than that of SiNWs/WS$_2$, qualitatively in accordance to the performance difference (Figure 4).

The values of elements in the equivalent circuit (inset of Figure 5a) can be extracted from the experimental EIS spectra by the data fitting, and the results of data fitting are shown in Table S3 (Supporting Information). The fitted values of $R_{ct,dl}$ are 98.12, 136, and 1323 Ω for SiNWs/WS$_3$, SiNWs/WS$_2$ and SiNWs, respectively. The $R_{ct,dl}$ of SiNWs/WS$_3$ is approximately 12 times smaller than that of the SiNWs sample, and 0.5 time smaller than that of SiNWs/WS$_2$, showing a good correlation with the remarkably enhanced photocurrent density in the SiNWs/WS$_3$ sample (Figure 4).

EIS experiments suggest that the performance enhancement of SiNWs loaded with WS$_3$ or WS$_2$ could be attributed to the electrocatalytic activity of WS$_3$ or WS$_2$, and the different performances between SiNWs/WS$_3$ and SiNWs/WS$_2$ could be ascribed to different electrocatalytic activities of WS$_3$ and WS$_2$. The difference between electrocatalytic activities of WS$_3$ and WS$_2$ was further confirmed by the polarization curves recorded with the same loading amount of WS$_3$ and WS$_2$ (loading amount: 0.285 mg/cm^2) on GCE, respectively. The corresponding J−V curves can be found in Figure 6, showing explicitly that the HER catalytic activity of WS$_3$ is higher than
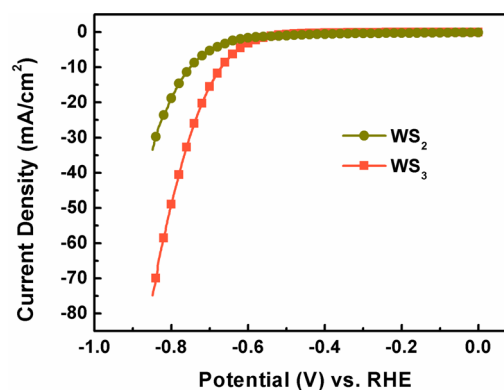

Figure 6. Polarization curves of WS$_2$ and WS$_3$ loading on GCE.

that of WS_2. WS_2 has a current density of 10 mA/cm^2 at an overpotential of 750 mV, whereas an overpotential for WS_3 of 670 mV is required for the same current density. At −800 mV vs RHE, the current density of WS_3 (48.9 mA/cm^2) is 2.6 times that of WS_2 (18.8 mA/cm^2). The evaluation of electrocatalytic activities of WS_3 and WS_2 confirms solidly that the superior photoelectrochemical performance of SiNWs/WS_3, in comparison with SiNWs/WS_2, can be attributed to better electrocatalytic activity of WS_3 than WS_2.

The active sites for HER in WS_2 and MoS_2 are the edges of the (−1010) plane,[13,17,27] except that density functional theory simulation suggests that the S edge (−1010) and W edge (−1010) are equally active in WS_2 whereas the Mo edge (−1010) is less active than the S edge (−1010) in MoS_2.[13] These edges have coordinatively unsaturated S and/or Mo (or W) atoms.[28,29] Accordingly, the catalytic activity of WS_2 and MoS_2 correlates heavily to the number of unsaturated S and/or W atoms (in other words, edge sites): the more unsaturated S and/or W atoms, the better HER performance. Several approaches have been developed to increase the number of unsaturated S and/or W atoms in MoS_x or WS_x. For example, Xie et al. demonstrated that disorder engineering and simultaneous oxygen incorporation in MoS_2 can offer abundant unsaturated S and dramatically enhance the HER activity.[30] Dai et al. revealed that breaking WS_2 nanotubes into nanoflakes by sonochemical exfoliation can remarkably increase the ratio of active sites and enhance HER performance.[18] Hu et al. showed that amorphous MoS_x exhibit superior HER activity in comparison with its crystalline counterpart. This superior performance has been attributed to the much more unsaturated sites because of amorphous structure.[28] It is further revealed that the better HER efficiency of amorphous MoS_2 is related to the presented of bridging S_2^{2-} or apical S^{2-} in an amorphous state.[29,31]

Our experiments have suggested that the larger η in SiNWs/WS_3, in comparison with SiNWs/WS_2, can be attributed to the better HER catalytic activity of WS_3 than WS_2 (Figures 5 and 6). In our experiment, WS_3 is amorphous with short-range ordering whereas WS_2 is crystalline (Figure 3). More unsaturated S and/or W active sites would exist in amorphous WS_3 or WS_3 with short-range ordered in comparison with crystalline WS_2, similar to those found by Hu et al.[28] Moreover, bridging S_2^{2-} or apical S^{2-} has been related to active species in MoS_x,[29,31] and it is reasonable to deduce that these sulfur species are also active species in tungsten sulfide. It is worth noting that bridging S_2^{2-} or apical S^{2-} is only detectible in amorphous WS_3, but not in crystalline WS_2 (Figure 2b), suggesting much more active species in WS_3 than in WS_2. On the other hand, the specific surface area of WS_3 powder is 19.226 m^2/g, whereas that of WS_2 powder is 5.130 m^2/g (Figure S7, Supporting Information). The larger specific surface area of WS_3 powder in comparison with WS_2 powder might also contribute positively to the better catalytic activity of WS_3 powder. Therefore, the different HER performances between WS_3 and WS_2 can be attributed to their different structural features and their different specific surface areas, which result in different numbers of HER active sites in samples,.

The Faradaic yield of SiNWs/WS_3 during H_2 production was also evaluated. The volume of generated gas was monitored via water displacement method when a potentiostatic electrolysis measurement was carried out. Figure 7 shows the comparison of the theoretical volume of hydrogen and the experimentally measured volume of hydrogen. It is shown that the Faradaic
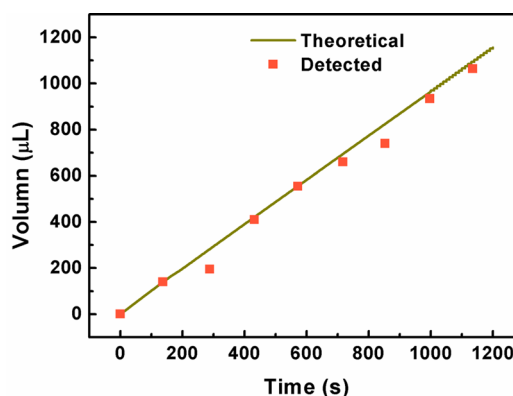
Figure 7. Current efficiency for H_2 production using SiNWs/WS_3 photocathode and performance stability of SiNWs/WS_3 photocathode. The theoretical line of H_2 volume was calculated by assuming that all electrons pass through the circuit are totally consumed by the reduction of H^+ into hydrogen (a 100% Faradaic H_2 production).

yield of H_2 production is quantitative within the experimental errors.

The stability of SiNWs/WS_3 and SiNWs/WS_2 was evaluated by potentiostatic electrolysis experiments. The results are shown in Figure S8 (Supporting Information). In the SiNWs/WS_3 sample, the current density decreases at the initial stage and then is nearly unchanged in the following measurement. For the SiNWs/WS_2 sample, a fast decrease of current density is found at the initial 10 min, and then the current density decreases very slowly with time.

4. CONCLUSIONS

SiNWs/WS_3 and SiNWs/WS_2 have been fabricated by combining drop coating and pyrolysis. SiNWs/WS_3 shows remarkably enhanced photoelectrochemical performance in comparison with SiNWs and SiNWs/WS_2. WS_3 is amorphous whereas WS_2 is crystalline. The enhancement of photoelectrochemical performance can be attributed to the electrocatalytic activity of WS_3, which reduces remarkably the charge transfer resistance at the photocathode/electrolyte interface and increases the HER kinetics. The superior electrocatalytic activity of WS_3 to WS_2 is also confirmed by corresponding polarization curves of WS_3 or WS_2 loaded on GCE, and can be attributed to the amorphous nature of WS_3, which results in more active sites than crystalline WS_2. A 100% Faradaic H_2 production is achieved on SiNWs/WS_3, and the photocurrent of SiNWs/WS_3 sample maintains at 90% of the initial value after 5 min of measurement. The method introduced here offers a convenient approach for the design and exploitation of materials exhibiting significantly enhanced photoelectrochemical hydrogen production capabilities.

■ ASSOCIATED CONTENT

ⓢ Supporting Information

Addition TGA/DSC, EDS, XPS, UV−vis spectra, experimental setup used to measure volume of H_2 during potentiostatic electrolysis, and list of performances of reported Si-based photocathode. This material is available free of charge via the Internet at http://pubs.acs.org.

■ AUTHOR INFORMATION

Corresponding Authors
*Zhipeng Huang. E-mail: zphuang@ujs.edu.cn.

*Chi Zhang. E-mail: chizhang@ujs.edu.cn. Fax: 86-511-8879-7815.

Notes

The authors declare no competing financial interest.

■ REFERENCES

(1) Walter, M. G.; Warren, E. L.; McKone, J. R.; Boettcher, S. W.; Mi, Q. X.; Santori, E. A.; Lewis, N. S. Solar Water Splitting Cells. *Chem. Rev.* **2010**, *110*, 6446−6473.

(2) Dominey, R. N.; Lewis, N. S.; Bruce, J. A.; Bookbinder, D. C.; Wrighton, M. S. Improvement of Photoelectrochemical Hydrogen Generation by Surface Modification of p-Type Silicon Semiconductor Photocathodes. *J. Am. Chem. Soc.* **1982**, *104*, 467−482.

(3) Reece, S. Y.; Hamel, J. A.; Sung, K.; Jarvi, T. D.; Esswein, A. J.; Pijpers, J. J. H.; Nocera, D. G. Wireless Solar Water Splitting Using Silicon-Based Semiconductors and Earth-Abundant Catalysts. *Science* **2011**, *334*, 645−648.

(4) Peng, K. Q.; Xu, Y.; Wu, Y.; Yan, Y. J.; Lee, S. T.; Zhu, J. Aligned Single-Crystalline Si Nanowire Arrays for Photovoltaic Applications. *Small* **2005**, *1*, 1062−1067.

(5) Garnett, E. C.; Yang, P. D. Silicon Nanowire Radial p-n Junction Solar Cells. *J. Am. Chem. Soc.* **2008**, *130*, 9224−9225.

(6) Boettcher, S. W.; Warren, E. L.; Putnam, M. C.; Santori, E. A.; Turner-Evans, D.; Kelzenberg, M. D.; Walter, M. G.; McKone, J. R.; Brunschwig, B. S.; Atwater, H. A.; Lewis, N. S. Photoelectrochemical Hydrogen Evolution Using Si Microwire Arrays. *J. Am. Chem. Soc.* **2011**, *133*, 1216−1219.

(7) McKone, J. R.; Warren, E. L.; Bierman, M. J.; Boettcher, S. W.; Brunschwig, B. S.; Lewis, N. S.; Gray, H. B. Evaluation of Pt, Ni, and Ni-Mo Electrocatalysts for Hydrogen Evolution on Crystalline Si Electrodes. *Energ Environ. Sci.* **2011**, *4*, 3573−3583.

(8) Lin, C. Y.; Lai, Y. H.; Mersch, D.; Reisner, E. Cu$_2$O Vertical Bar NiO$_x$ Nanocomposite as An Inexpensive Photocathode in Photoelectrochemical Water Splitting. *Chem. Sci.* **2012**, *3*, 3482−3487.

(9) Hou, Y. D.; Abrams, B. L.; Vesborg, P. C. K.; Bjorketun, M. E.; Herbst, K.; Bech, L.; Setti, A. M.; Damsgaard, C. D.; Pedersen, T.; Hansen, O.; Rossmeisl, J.; Dahl, S.; Norskov, J. K.; Chorkendorff, I. Bioinspired Molecular Co-Catalysts Bonded to A Silicon Photocathode for Solar Hydrogen Evolution. *Nat. Mater.* **2011**, *10*, 434−438.

(10) Seger, B.; Laursen, A. B.; Vesborg, P. C. K.; Pedersen, T.; Hansen, O.; Dahl, S.; Chorkendorff, I. Hydrogen Production Using a Molybdenum Sulfide Catalyst on a Titanium-Protected n plus p-Silicon Photocathode. *Angew. Chem., Int. Ed.* **2012**, *51*, 9128−9131.

(11) Huang, Z. P.; Wang, C. F.; Pan, L.; Tian, F.; Zhang, X. X.; Zhang, C. Enhanced Photoelectrochemical Hydrogen Production Using Silicon Nanowires@MoS$_3$. *Nano Energy* **2013**, *2*, 1337−1346.

(12) Sobczynski, A.; Yildiz, A.; Bard, A. J.; Campion, A.; Fox, M. A.; Mallouk, T.; Webber, S. E.; White, J. M. Tungsten Disulfide: A Novel Hydrogen Evolution Catalyst for Water Decomposition. *J. Phys. Chem.* **1988**, *92*, 2311−2315.

(13) Bonde, J.; Moses, P. G.; Jaramillo, T. F.; Norskov, J. K.; Chorkendorff, I. Hydrogen Evolution on Nano-Particulate Transition Metal Sulfides. *Faraday Discuss.* **2008**, *140*, 219−231.

(14) Jing, D. W.; Guo, L. J. WS$_2$ Sensitized Mesoporous TiO$_2$ for Efficient Photocatalytic Hydrogen Production from Water under Visible Light Irradiation. *Catal. Commun.* **2007**, *8*, 795−799.

(15) Zong, X.; Han, J. F.; Ma, G. J.; Yan, H. J.; Wu, G. P.; Li, C. Photocatalytic H$_2$ Evolution on CdS Loaded with WS$_2$ as Cocatalyst under Visible Light Irradiation. *J. Phys. Chem. C* **2011**, *115*, 12202−12208.

(16) Wu, Z. Z.; Fang, B. Z.; Bonakdarpour, A.; Sun, A. K.; Wilkinson, D. P.; Wang, D. Z. WS$_2$ Nanosheets as A Highly Efficient Electrocatalyst for Hydrogen Evolution Reaction. *Appl. Catal., B* **2012**, *125*, 59−66.

(17) Voiry, D.; Yamaguchi, H.; Li, J. W.; Silva, R.; Alves, D. C. B.; Fujita, T.; Chen, M. W.; Asefa, T.; Shenoy, V. B.; Eda, G.; Chhowalla, M. Enhanced Catalytic Activity in Strained Chemically Exfoliated WS$_2$ Nanosheets for Hydrogen Evolution. *Nat. Mater.* **2013**, *12*, 850−855.

(18) Choi, C. L.; Feng, J.; Li, Y. G.; Wu, J.; Zak, A.; Tenne, R.; Dai, H. J. WS$_2$ Nanoflakes from Nanotubes for Electrocatalysis. *Nano Research* **2013**, *6*, 921−928.

(19) Huang, Z. P.; Geyer, N.; Werner, P.; de Boor, J.; Gosele, U. Metal-Assisted Chemical Etching of Silicon: A Review. *Adv. Mater.* **2011**, *23*, 285−308.

(20) Peng, K. Q.; Yan, Y. J.; Gao, S. P.; Zhu, J. Synthesis of Large-Area Silicon Nanowire Arrays via Self-Assembling Nanoelectrochemistry. *Adv. Mater.* **2002**, *14*, 1164−1167.

(21) van der Vlies, A. J.; Kishan, G.; Niemantsverdriet, J. W.; Prins, R.; Weber, T. Basic Reaction Steps in the Sulfidation of Crystalline Tungsten Oxides. *J. Phys. Chem. B* **2002**, *106*, 3449−3457.

(22) Paola, D. A.; Palmisano, L.; Venezia, A. M.; Augugliaro, V. Coupled Semiconductor Systems for Photocatalysis. Preparation and Characterization of Polycrystalline Mixed WO$_3$/WS$_2$ Powders. *J. Phys. Chem. B* **1999**, *103*, 8236−8244.

(23) Tran, P. D.; Pramana, S. S.; Kale, V. S.; Nguyen, M.; Chiam, S. Y.; Batabyal, S. K.; Wong, L. H.; Barber, J.; Loo, J. Novel Assembly of an MoS$_2$ Electrocatalyst onto a Silicon Nanowire Array Electrode to Construct a Photocathode Composed of Elements Abundant on the Earth for Hydrogen Generation. *Chem.—Eur. J.* **2012**, *18*, 13994−13999.

(24) Oh, I.; Kye, J.; Hwang, S. Enhanced Photoelectrochemical Hydrogen Production from Silicon Nanowire Array Photocathode. *Nano Lett.* **2013**, *12*, 298−302.

(25) Lopes, T.; Andrade, L.; Ribeiro, H. A.; Mendes, A. Characterization of Photoelectrochemical Cells for Water Splitting by Electrochemical Impedance Spectroscopy. *Int. J. Hydogen Energy* **2010**, *35*, 11601−11608.

(26) Merki, D.; Vrubel, H.; Rovelli, L.; Fierro, S.; Hu, X. L. Fe, Co, and Ni Ions Promote the Catalytic Activity of Amorphous Molybdenum Sulfide Films for Hydrogen Evolution. *Chem. Sci.* **2012**, *3*, 2515−2525.

(27) Jaramillo, T. F.; Jørgensen, K. P.; Bonde, J.; Nielsen, J. H.; Horch, S.; Chorkendorff, I. Identification of Active Edge Sites for Electrochemical H$_2$ Evolution from MoS$_2$ Nanocatalysts. *Science* **2007**, *317*, 100−102.

(28) Merki, D.; Fierro, S.; Vrubel, H.; Hu, X. L. Amorphous Molybdenum Sulfide Films as Catalysts for Electrochemical Hydrogen Production in Water. *Chem. Sci.* **2011**, *2*, 1262−1267.

(29) Yan, Y.; Xia, B. Y.; Ge, X. M.; Liu, Z. L.; Wang, J. Y.; Wang, X. Ultrathin MoS$_2$ Nanoplates with Rich Active Sites as Highly Efficient Catalyst for Hydrogen Evolution. *ACS Appl. Mater. Interfaces* **2013**, *5*, 12794−12798.

(30) Xie, J. F.; Zhang, J. J.; Li, S.; Grote, F.; Zhang, X. D.; Zhang, H.; Wang, R. X.; Lei, Y.; Pan, B. C.; Xie, Y. Controllable Disorder Engineering in Oxygen-Incorporated MoS$_2$ Ultrathin Nanosheets for Efficient Hydrogen Evolution. *J. Am. Chem. Soc.* **2013**, *135*, 17881−17888.

(31) Chang, Y. H.; Lin, C. T.; Chen, T. Y.; Hsu, C. L.; Lee, Y. H.; Zhang, W. J.; Wei, K. H.; Li, L. J. Highly Efficient Electrocatalytic Hydrogen Production by MoS$_x$ Grown on Graphene-Protected 3D Ni Foams. *Adv. Mater.* **2013**, *25*, 756−760.